Enhancement of the spin-glass transition temperature through *pd*-orbital hybridization in $Zn_{1-x}Mn_xTe$

A. R. Alcantara,[1] S. Barrett,[1] D. Matev,[1] I. Miotkowski,[2] A. K. Ramdas,[2] T. M. Pekarek,[1] and J. T. Haraldsen[1]
[1]*Department of Physics, University of North Florida, Jacksonville, Florida 32224, USA*
[2]*Department of Physics, Purdue University, West Lafayette, Indiana 47907, USA*

(Received 26 March 2021; revised 7 September 2021; accepted 10 September 2021; published 22 September 2021)

To gain insight into the spin-glass state of diluted magnetic semiconductors, we have examined the magnetic and electronic properties of $Zn_{1-x}Mn_xTe$ using density-functional theory as well as performed magnetization measurements on the $x = 0.43$ and 0.55 systems to demonstrate a clear spin-glass transition consistent with previous literature. Using a generalized gradient approximation, we investigate the electronic and magnetic properties for $x = 0$, 0.075, 0.15, 0.25, and 0.50 doping levels using the magnetic moment of Mn^{2+} as guide for the dependence of the Hubbard onsite potential on the electronic structure. Simulations on both ferromagnetic (FM) and antiferromagnetic (AFM) configurations yield a distinct AFM ground-state preference, which is consistent with a zero-magnetic-moment spin-glass state. Here an onsite potential of up to 8 eV on the Mn 3*d* orbitals is needed to harden the magnetic moment toward $S = 5/2$. From our analysis of the electronic structure evolution with doping and onsite potential, we confirm the semiconducting state of the Mn-doped ZnTe as well as show that the presence of Mn incorporated into the ZnTe matrix at the Zn lattice site produces magnetic interactions through the Te ions with a distinct Te-Mn *pd*-orbital hybridization. Furthermore, we show that this hybridization is activated with the Mn doping above 0.25 concentration, which corresponds to the doping level in which the spin-glass transition begins to rise. Therefore, it is likely that the coupling of *pd*-orbital hybridization of the Mn and Te *p* orbitals is a precursor to the enhancement of the spin-glass transition temperature.

DOI: 10.1103/PhysRevB.104.104423

I. INTRODUCTION

Over the past few decades, the spin-glass states have provided an interesting conundrum with magnetic materials as they exhibit small but measurable magnetic interactions while providing no distinct magnetic order. Similarly to paramagnets, the magnetic moments in spin glasses are randomly oriented in a zero magnetic field environment and aligned while in a finite applied magnetic field. However, unlike a paramagnet, the spin glass does not immediately return to a net zero magnetic moment when the applied field is removed [1,2]. Instead, it produces a remnant magnetic memory with a divergently slower relaxation time. This magnetic decay over time opens the door to the possibility of technology potential for spin-glass materials, not necessary in long-term information storage, but in short-term, low-energy memory and processing power [3–6].

Currently, the study of the interactions and complexity of spin-glass behavior has led to understanding in combinatorial mathematics used for investigation of neural networks and quantum computation [7], which can possess benefits in difficult modern real-world problems. The understanding of networking interactions through spin-glass materials demonstrates a need for solidifying the foundations of interactions within them. The difficulty with understanding and researching spin-glass materials is that they do not have a distinct electronic signature or pattern. The presence of this unique magnetic state can be determined through analysis of a material's magnetic behavior. However, these measurements do not provide a distinct electronic state. As shown in Fig. 1, spin-glass materials can be metals, insulators, and semiconductors [8–23,25–32], where one clue to their formation comes from the fact that the transition temperature of spin glasses increases with carrier density and electronic mobility, which indicates a need for distinct orbital interactions.

The critical temperatures necessary for a transition in magnetic state are detailed in Fig. 1, where spin-glass transition temperature as function of doping concentration is shown. Here metals have a dramatic increase in transition temperature due to higher electron mobility through the conduction band provided through direct orbital interactions [1]. Semiconducting materials and insulators have distinctly lower transition temperatures compared to metals since their interactions have to move through an intermediary of nonmetallic anions. Therefore, they rely on spin interactions through orbital superexchange in a diluted magnetic environment. Since insulating spin glasses do not exhibit any larger amount of change in the transition temperatures between doping concentrations, the ability to examine change in the orbital interactions for the spin-glass state will be challenging. Therefore, the diluted magnetic semiconductor (DMS) materials may provide a greater level of insight into the orbital preferences as well as the preferred coupling.

Monochalcogenide materials of the MX variety are of particular interest to the condensed matter community due to their interesting electronic properties that has been shown to lead to exotic superconductivity and/or magnetic states

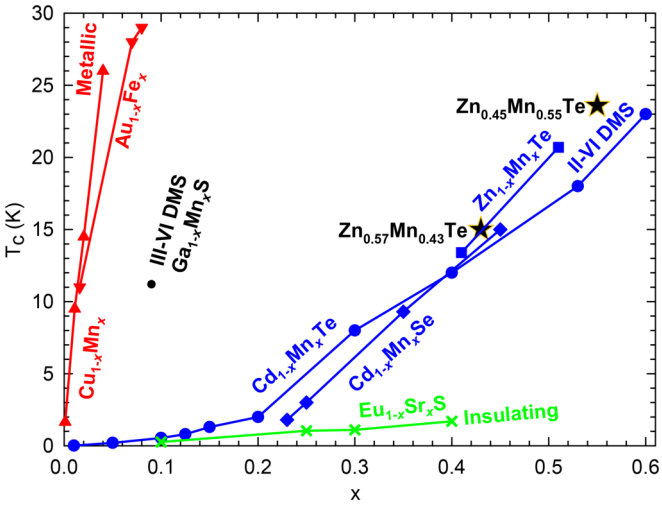

FIG. 1. Critical temperature T_c versus concentration x for representative metallic, semiconducting, and insulating materials [8–24]. Newly established T_c data for $Zn_{0.57}Mn_{0.43}Te$ and $Zn_{0.45}Mn_{0.55}Te$ are represented by stars.

[8–10,25–32]. Here M is a transition metal ion and X is a chalcogenide (e.g., S, Se, and Te). Many of these materials produce robust semiconducting states and have been used in solar cells and electronic components. Doping these chalcogenide materials with moderate amounts of magnetic transition-metal elements have been shown to produce diluted magnetic semiconductors [11–23]. More interestingly, many of these materials exhibit spin-glass behavior.

One material of interest is ZnTe, which is a semiconducting material with a direct band gap of 2.26 eV [8] and a cubic lattice. Given the semiconducting nature of ZnTe, it is typically used in the creation of solar cells when deposited on GaAs [33]. This is particularly attractive to innovators in the field of optoelectronics, where it is feasible that this material could replace typical silicon devices. Another benefit of this material is the ease and crystallographic precision with which it can doped with other elements. When doped with transition-metal atoms such as Mn, $Zn_{1-x}TM_xTe$ becomes a diluted magnetic semiconductor with a spin-glass phase at low temperatures. Additionally, the band gap of $Zn_{1-x}TM_xTe$ increases with Mn concentration [34], which provides the potential for semiconducting tunability.

Previous density-functional theory (DFT) studies on $Zn_{1-x}TM_xTe$ have looked mainly at the magnetic and optical properties with various transition metals [12]. While this particular study examined the low concentration of transition metal dopants, it shows similar insights within the narrow minimal-doping regime.

Therefore, in this study, we examine the electronic and magnetic properties of Mn-doped ZnTe through the utilization of magnetization measurements and density-functional calculations. Magnetization measurement were performed on single crystalline $Zn_{1-x}Mn_xTe$ ($x = 0.43$ and 0.55) samples to confirm the spin-glass state of this material and characterize the transition temperature. Additionally, we used density-functional theory to simulate the electronic and magnetic states of the material to examine the effects of orbital interactions with doping levels of $x = 0.25$ and 0.50. Through an examination of the electronic band structure and density of states for various onsite potentials, we find that highest occupied molecular orbital levels in the valence band are dominated by the Te p orbitals. However, as Mn is added to the system, the Mn d orbitals become increasingly more dominant in the lowest unoccupied molecular orbital conduction bands. This allows for potential transitions between Te and Mn through p-d hybridization of the orbitals, which correlates well with the observed increase of T_c around $x = 0.20$ in many materials.

II. METHODOLOGY

Magnetic measurements were taken on single crystalline $Zn_{1-x}Mn_xTe$ ($x = 0.43$ and 0.55 with $\delta x \pm 0.03$) samples that were grown by a modified Bridgman method. The magnetization was investigated using a Quantum Design MPMS XL7 superconducting quantum interference device magnetometer at temperatures between 5 and 400 K in fields up to 7 T.

Calculations were performed using DFT through the utilization of the Quantum Atomistix Toolkit by Quantumwise [35,36]. Starting with the standard zinc telluride structure, Zn atoms were replaced with Mn atoms at random sites to produce a general doping of 7.5, 15, 25, and 50% Mn atoms. Using a geometry optimization, the structures were relaxed to confirm the zinc blende structure as the ground-state configuration, which is in agreement with previous x-ray analysis of bulk crystals for these concentrations [37]. Multiple structures with the same doping level were analyzed with little to no change in the electronic structure.

Using a spin-polarized generalized gradient approximation in the Perdew, Burke, and Ernzerhof functional was applied using a $10 \times 10 \times 10$ k-point sampling of ZnTe and $Zn_{1-x}Mn_xTe$ with $x = 0.075$, 0.15, 0.25, and 0.50. Furthermore, calculations were performed using a Hubbard onsite potential of 0, 2, 4, 6, and 8 eV on the Mn $3d$ orbitals to help localize the magnetic moments and produce the correct stoichiometric oxidation state of Mn^{2+} expected for this material. Since the Mn^{2+} oxidation state produces a high-spin state of $S = 5/2$ on the Mn atom, we find that the higher onsite potential of 8 eV reproduces the proper gap and magnetic moment for Mn-doped ZnTe. While these U values seem to be large in comparison to transition-metal oxide systems, the range of 5 to 9 eV are typical values found for diluted magnetic semiconductors [38–43]. From the electronic structure calculations, the electronic band structure, density of states (DOS), and magnetic and electron density are determined. As shown in Table I, an examination of the total energy for the ferromagnetic (FM) and antiferromagnetic (AFM) configurations demonstrated that the ground state is AFM since the change in energy favors that configuration.

III. MAGNETIZATION MEASUREMENTS

We previously confirmed that $Zn_{0.49}Mn_{0.51}Te$ was a spin glass using a universal scaling fit to the nonlinear magnetization [shown in the upper inset of Fig. 2(a)]. Here the parameters γ and β are critical exponents for the universal scaling fit and $\epsilon = (T - T_c)/T_c$ is the reduced temperature

TABLE I. Comparison of the total energy for the ferromagnetic (FM) and antiferromagnetic (AFM) configurations for the $U = 8$ calculations. The energy difference shows that the AFM state is the energetically stable ground state.

x	E_{FM} (eV)	E_{AFM} (eV)	$\Delta E = E_{\mathrm{AFM}} - E_{\mathrm{FM}}$ (meV)
0.25	−15,156.7207	−15,156.7286	-7.9 ± 0.3
0.50	−13,301.8774	−13,301.9125	-35.1 ± 0.3

[22]. However, there are limited experimental results for transition temperatures for $Zn_{1-x}Mn_xTe$ at high concentrations. Therefore, to gain further insight in the notable increase in the T_C for the $Zn_{1-x}Mn_xTe$ system for concentrations above $x = 0.2$ shown in Fig. 1, we examined the zero-field-cooled (ZFC) and field-cooled (FC) magnetization versus temperature measurements for $x = 0.43$ and 0.55, respectively [shown in Figs. 2(a) and 2(b)].

These values for x were estimated using Fig. 1, where the experimentally observed values for T_c in this paper were compared to a linear fit to the previously published data [11–23]. Magnetization measurements confirm the onset of the spin-glass transition due to the presence of a prominent cusp seen at 15.0 ± 0.2 K for the $x = 0.43$ data taken in 0.0200 T [Fig. 2(a)] and 23.6 ± 0.2 K for the $x = 0.55$ data taken in 0.0300 T [Fig. 2(b)]. For temperatures above the spin-glass phase, distinct paramagnetic behavior is observed from 30 to 400 K for both samples (shown in the lower inset figures with a field strength of 1 and 2 T).

The lower insets of Fig. 2 also show that the cusps shift to lower temperatures in higher fields. The considerable drop in transition temperature (e.g., above 0.5 T) is characteristic of a spin-glass material as the field energy is large enough to effect the exchange interactions of 1–2 meV.

A series of measurements were made in different applied fields to study the shift in the prominent peak temperature observed in Fig. 2. Figure 3 shows the field dependence of the spin-glass transition cusp for $x = 0.43$ and 0.55. For applied fields below 0.3000 T for $x = 0.55$ and below 0.0600 T for $x = 0.43$, the peak temperature remains constant indicating

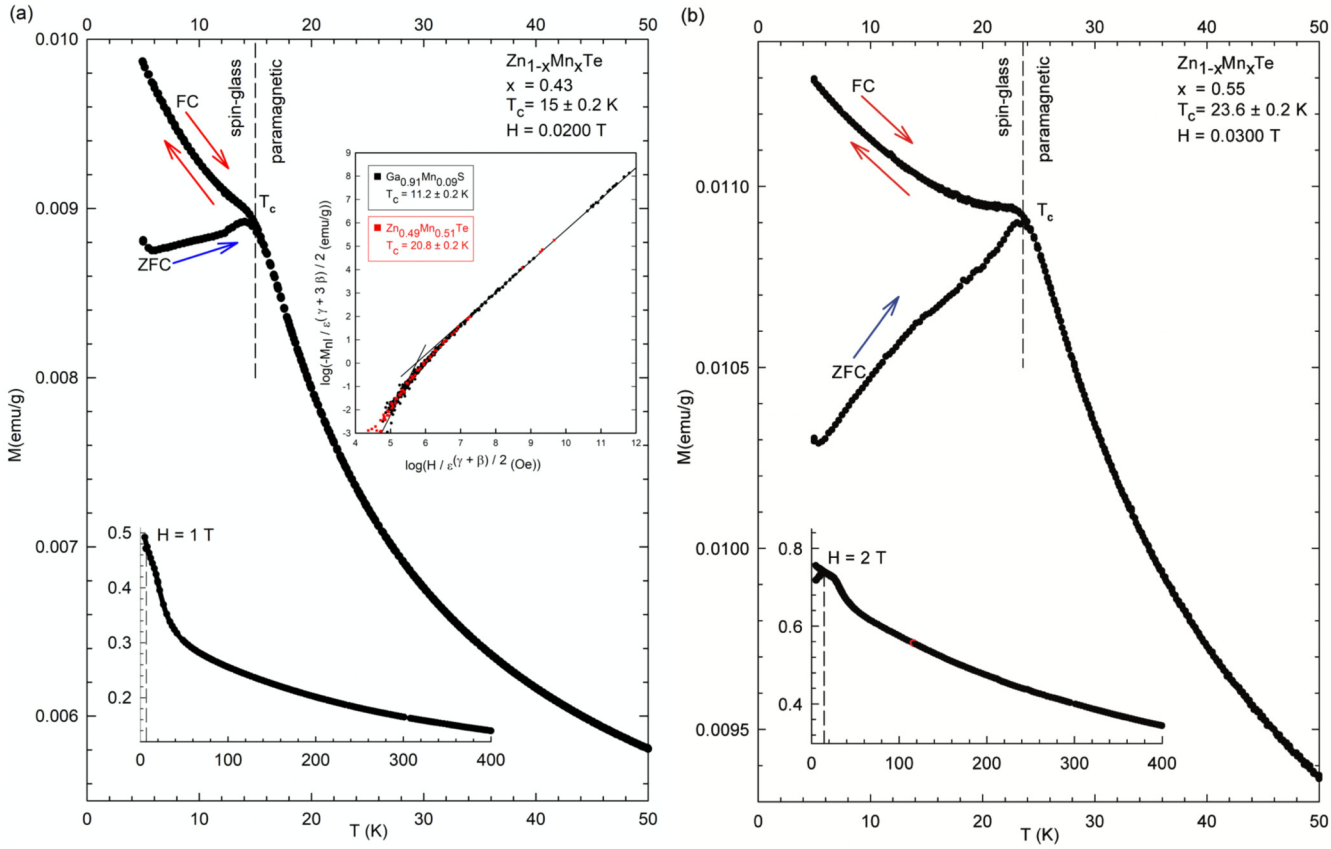

FIG. 2. (a) Zero-field-cooled (ZFC) and field-cooled (FC) magnetization versus temperature for $Zn_{0.57}Mn_{0.43}Te$. A prominent cusp is seen at 15.0 ± 0.2 K for the 0.0200 T data. (b) ZFC and FC magnetization versus temperature for $Zn_{0.45}Mn_{0.55}Te$. A prominent cusp is seen at 23.6 ± 0.2 K for the 0.0300-T data. Paramagnetic behavior is observed from 30 to 400 K for both samples. This is shown in the inset figures with a field strength of 1 and 2 T, respectively, where there is a flattened tail above the spin-glass transition temperature. This indicates a transition to the spin-glass phase for both concentrations. The cusp is observed to shift to lower temperatures in the 1- and 2-T fields. The top inset of (a) shows a universal scaling fit of nonlinear magnetization for our previous data on $Ga_{0.91}Mn_{0.09}S$ and $Zn_{0.49}Mn_{0.51}Te$ that was able to definitively confirm the transition to the spin-glass state [11,22].

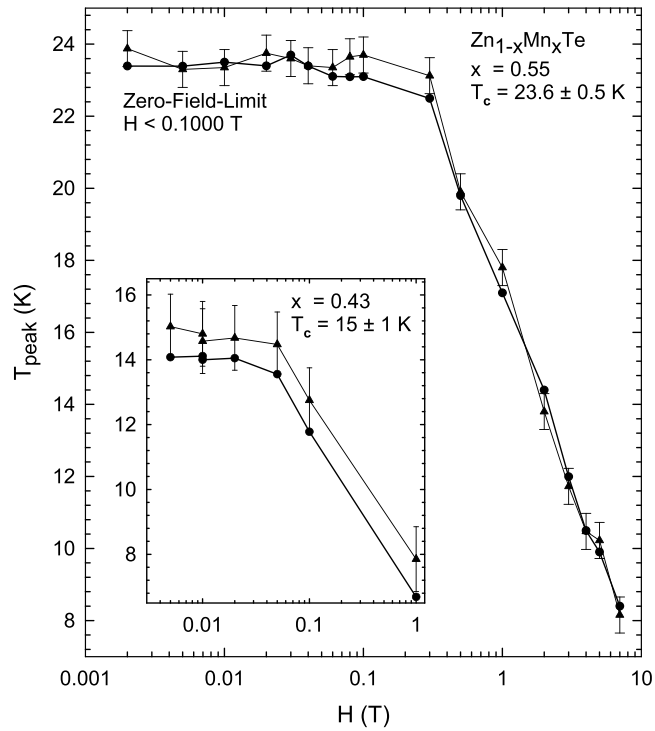

FIG. 3. Peak temperature versus applied field H for $Zn_{0.45}Mn_{0.55}Te$, while inset shows the values for the $Zn_{0.57}Mn_{0.43}Te$ sample. Triangle points indicate estimated value for T_c for the FC data with error bars, while the circles show data points taken for the peak value in the cusp of the ZFC trace.

the zero-field-limit has been reached. Here the sudden drop off of magnetization at higher field is a distinct feature of spin-glass materials. This is further captured in Fig. 4, where the normalized magnetization is shown for $Zn_{0.45}Mn_{0.55}Te$ as

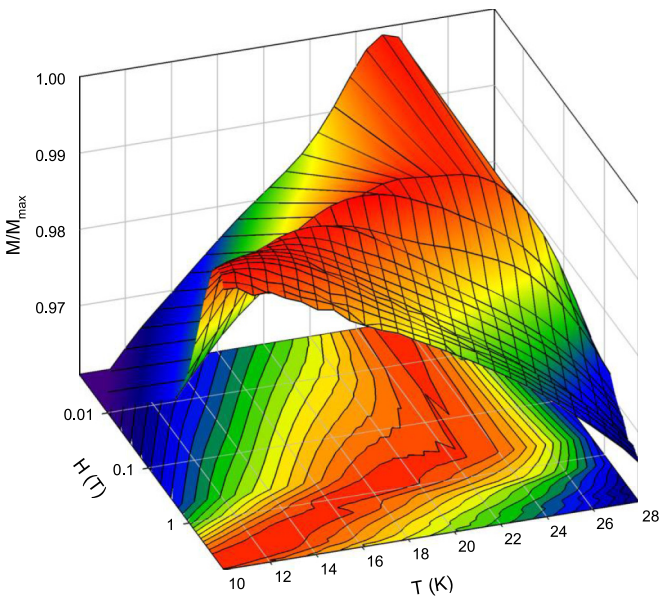

FIG. 4. Normalized magnetization as a function of applied magnetic field and temperature for $Zn_{0.45}Mn_{0.55}Te$. Note the log scale on the $H(T)$ axis.

a function of applied magnetic field and temperature, which details the field-cooled magnetization for the $x = 0.55$ crystal in the vicinity of the spin-glass transition.

With this prominent upward shift of T_C with doping characterized (Fig. 1), the underlying microscopic cause for it remains unsolved. Typically, this is just explained through a phenomenological power law of the transition temperature. To explore this further, we employ density-functional theory to investigate the electronic and orbital contributions in an attempt to provide increase clarity to the effects of magnetic doping of semiconductors.

IV. DENSITY-FUNCTIONAL ANALYSIS

Figure 5 shows the evolution of the electronic band structure and DOS for Mn doping of ZnTe with various onsite potentials on the 3*d* orbitals of Mn. An analysis of this nonmagnetic structure, is shown under the influence of Mn doping for 0.25 [Fig. 5(b)] and 0.50 [Fig. 5(c)] concentrations. The DOS can be broken into partial DOS (PDOS) and local DOS (LDOS) distinctions to detail the effects of orbital and atomic contributions for the different compounds.

The electronic band structure for ZnTe shows a distinct direct semiconducting band gap [Fig. 5(a)]. Through an examination of the breakdown for the DOS, the Zn atoms provide only *s*- and *p*-orbital contributions to the DOS, while the Te atom contribute mainly *p* and *d* orbitals. Therefore, it is not surprising that majority of the DOS comes from the overlap of *p* orbitals. Furthermore, the spin-polarized calculations show no formation of a magnetic moment on either Zn nor Te, which is consistent with being nonmagnetic.

The electronic structure and DOS for the Mn-doped ZnTe are shown for concentrations of 0.25 [Fig. 5(b)] and 0.50 [Fig. 5(c)] with various Hubbard onsite potentials applied to the Mn 3*d* orbitals. Multiple configurations of Mn doping were simulated for each concentration as well as multiple magnetic configurations. Therefore, the data shown is only that of the configuration illustrated in the figure. In general, the AFM configurations were always a lower energy ground state (see Table I), where the systems with the smallest net magnetic moment had the lowest energy, consistent with the formation of a zero magnetic moment spin-glass state. Further studies using noncollinear spin states may provide further insight.

The electronic bands in Fig. 5 include both spin up and spin down bands. The zero net magnetic moment of ZnTe and the symmetry of the AFM state in the $x = 0.25$ case allows for the bands to be degenerate or close to degenerate. In the $x = 0.50$ case, the asymmetry of the magnetic moments breaks the degeneracy even though the system has zero net magnetic moment in the AFM case.

Figure 6 shows the calculated magnetic moment on the Mn atoms [Fig. 6(a)] and the estimated direct band gap from electronic structure [Fig. 6(b)] as functions of the Hubbard onsite potential. It is clear from the data that increasing the onsite hardens the magnetic moment and increases the calculated band gap. Figure 6(a) shows a value of 4.4 μ_B at $U = 0$ eV, which indicates a $S = 2$ state for the Mn, and is not consistent with the stoichiometric value of $S = 5/2$. However, after adjusting U to 8 eV, there is a substantial increase in the magnetic moment to around 5.4 μ_B.

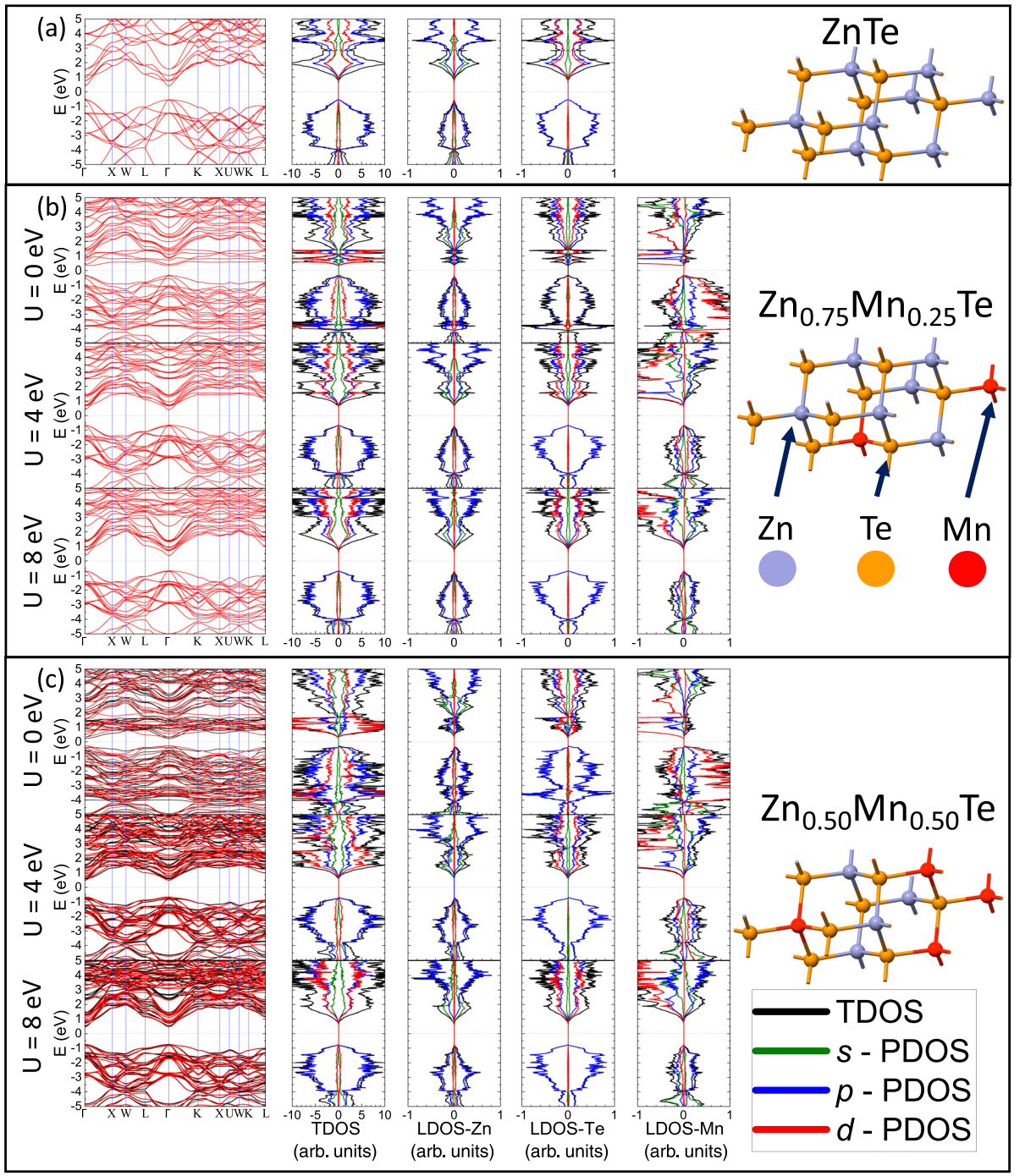

FIG. 5. The electronic band structure and density of states for ZnTe (a) as well as 0.25 (b) and 0.50 (c) doping concentrations of Mn-doped ZnTe with Hubbard-U interaction of 0, 4, and 8 eV. The Mn-doped structures are in the AFM configuration.

Furthermore, from Fig. 6(b), the band gap for the concentration of $x = 0.50$ compound is smaller than the $x = 0.25$ with a $U = 0$ eV, which does not agree with the experimental measurements and trends [34]. However, as with the magnetic moment, this was corrected with the increase U to 8 eV. Figure 5 shows the electronic structure calculations with $U =$ 0, 4, and 8 eV for $x = 0.25$ and 0.50 doping concentrations compared with ZnTe shown in Fig. 5(a). Using $x = 0.25$ doped Mn substituted in the Zn sites shown without a Hubbard-U potential, impurity bands loosely fall toward the Fermi level and many valence bands are flat representing poor carrier mobility. Introducing a U of 4 eV, the electric band structure is more defined and enlarges the band gap. This produces more availability in charge carrier density. This trend continues for $U = 8$ eV. Therefore, we can be fairly confident in the analysis of the $U = 8$ eV data providing most insight into the electronic states of Mn-doped ZnTe.

Examining the total DOS (TDOS) for 0.25 doping [Fig. 5(b)], p orbitals continue to dominate the structure in the conduction bands contributed from Zn and Mn. Te p

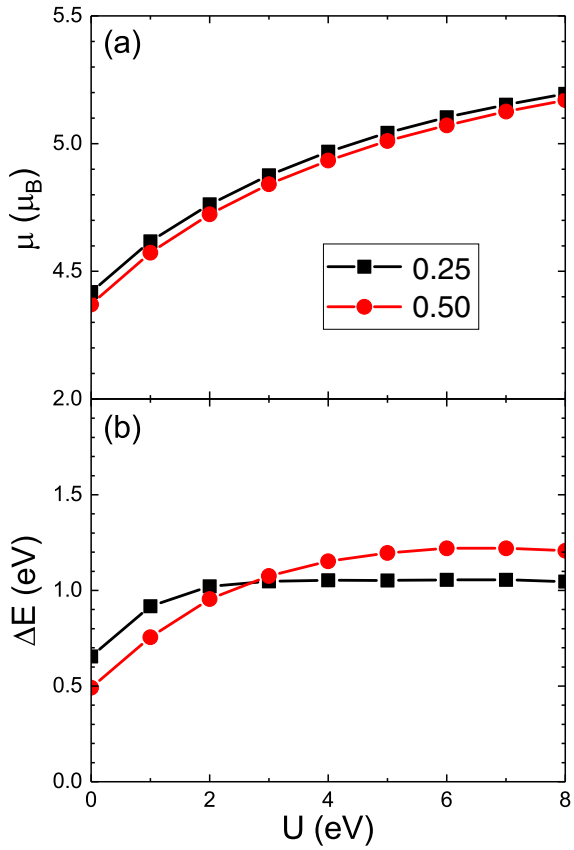

FIG. 6. Hubbard-U interaction for $x = 0.25$ and 0.50 doping of Mn. The vertical axis in (a) is the calculated magnetic moment and (b) band gap energy as a function of Hubbard-U.

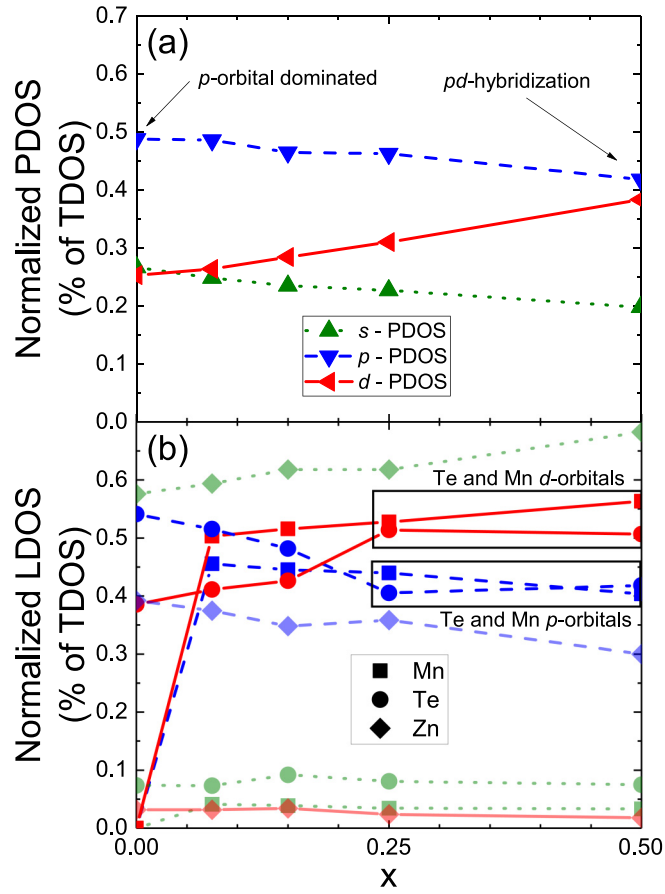

FIG. 7. (a) Normalized partial density of states (PDOS) at 2.0 eV for the s (dotted green lines with up-triangles), p (dashed blue lines with down-triangles), and d orbitals (solid red lines with left-triangles) as a function of Mn concentration. (b) Normalized local density of states (LDOS) for the Mn atoms (squares), Te (circles), and Zn (diamonds) for the s (dotted green lines), p (dashed blue lines), and d orbitals (solid red lines) as a function of Mn concentration. For the $x = 0.07$, 0.15, 0.25, and 0.50 concentration, $U = 8$ eV. Please note that the $x = 0.07$ and 0.15 data points were calculated using a larger 54 atom unit cell to assure the proper doping concentration. Additionally, the same DFT parameters as the $x = 0.25$ and 0.50 were used. Since the DOS analysis is normalized to the total DOS, the data are comparable to the 0.25 and 0.50 DOS data.

orbitals hold majority of the density in the valence bands. Additionally, the s orbitals weakly contribute to both valence and conduction bands.

In the $x = 0.50$ doped case [Fig. 5(c)], the electronic band structure shows both up and down bands. This separation is caused by the slight imbalance of magnetic impurities randomly interacting with local atoms. In a noncollinear system, these bands would be more degenerate. However, this does not have an effect on the analysis. Similarly to the $x = 0.25$ case, Te p orbitals in the valence bands are a large contribution to the TDOS, and s orbitals in the conduction band provide only a weak contribution to the system. However, the TDOS for the 50% doping exhibits larger contribution from d orbitals in the conduction bands. By taking a closer look at the LDOS, it is shown that Mn d orbitals exhibit substantial presence in the conduction bands, and Zn continues to provide only s and p orbitals to the overall system.

Overall, in ZnTe, the Te and Zn interact through a mainly p-orbital coupling. However, as Mn is added to the system, the d and p orbitals of the Mn hybridize and begin to interact with the Te. Increasing Mn doping seems to increase this interaction above 0.25 Mn doping, which indicates a shift in the Te away from the Zn p-orbital interaction and toward to the Mn pd hybridized interaction.

These changes in the orbital characteristics can be observed through an analysis of the normalized PDOS and LDOS (at 2.0 eV and $U = 8$ eV) for various doping levels of Mn in ZnTe (shown in Fig. 7). Figure 7(a) shows that, in the absence of Mn, the ZnTe matrix is dominated by p-orbital interactions. However, once the Mn is introduced into the system, the d orbitals of the system become relevant.

In Fig. 7(b), this analysis is broken down to the local level. Here, it is clear that the Te p and d orbitals are shifting their interactions toward an overlap of the p- and d orbitals of the Mn, which is effectively shutting out the Zn orbitals. We have highlighted the Mn and Te p- and d-orbital contributions to the DOS to make the trends clearer.

To further understand the DOS analysis in Fig. 7, we ran additional simulations on a larger 54-atom supercell of ZnTe with $x = 0.075$ and 0.15 doping concentrations of Mn. These

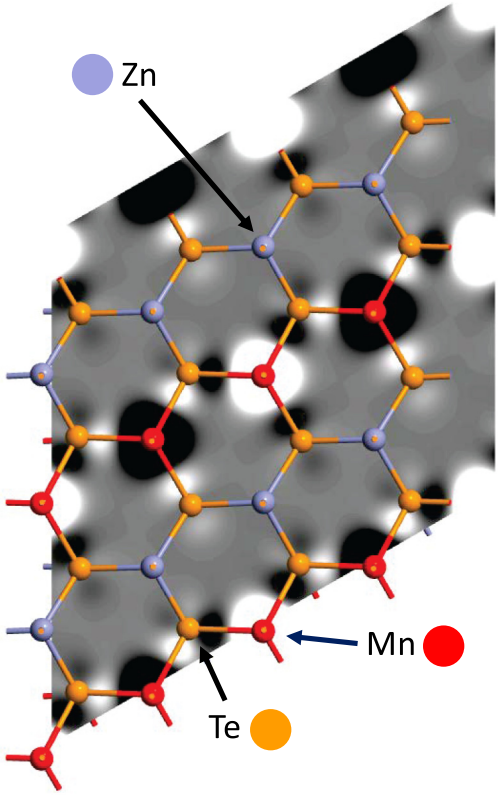

FIG. 8. Electron density difference between the spin-up (white) and spin-down (black) channels for the 50% concentration (U = 8 eV) that highlights the coupling between the Mn and Te pd hybridized orbitals. Here Zn atoms are purple, Te is gold, and Mn is red.

data points clarify the orbital transitions between the mother compound and $x = 0.25$ doping concentration.

V. DISCUSSION

As shown in Fig. 7(b), the shaded boxes highlight that the introduction of Mn separates the Te DOS from the Zn DOS, which produces a stronger interaction between the Mn and Te p and d orbitals at high concentrations and allows for a greater exchange of electrons throughout the system; effectively shutting out the Zn orbital interactions.

Looking at the electron density difference for the 0.50 case (shown in Fig. 8), the spin-up and spin-down moments are highlighted to exhibit possible coupling between the Mn and Te pd hybridization as suggested from Fig. 5. Darker portions represent down electron spins, brighter portions represent up spins. Here most of the electron density interaction is shown around Mn and Te, whereas Zn has little to no contribution, as previously stated.

The presence of d-orbital interactions due to the introduction of Mn in the ZnTe matrix is not that surprising. Using photoemission spectroscopy, Bhattacharjee *et al.* showed that Mn will produce exchange interactions in $Cd_{1-x}Mn_xTe$ at low doping due to increased overlap of Mn d orbitals in the valence bands [44], which is consistent with our analysis.

Overall, this analysis provides a more microscopic understanding of the evolution of the p- and d-orbital interactions with the increased presence of transition metal ions in DMS spin-glass materials. Through the combination of this work and the aforementioned previous literature, the presence of Mn d orbitals provides superexchange pathways through the ZnTe matrix, which increases the overall interaction strength, as shown in Table I. As the system interactions become more long-ranged, the spin-glass state can become more robust leading to a significant shift in the spin-glass transition temperature. This is likely due to the thermal population of hybridized orbitals in the conduction bands that become more active at the transition temperature. For Mn-doped ZnTe, this shift in transition temperature seems to be above 20% doping concentration, which is consistent with the critical temperature plot in Fig. 1.

VI. CONCLUSION

In conclusion, we experimentally investigated the magnetic properties of $Zn_{0.57}Mn_{0.43}Te$ and $Zn_{0.45}Mn_{0.55}Te$. We find a prominent cusps indicating a transitions to the spin-glass state at 15.0 K for $Zn_{0.57}Mn_{0.43}Te$ and at 23.6 K for $Zn_{0.45}Mn_{0.55}Te$, expanding the temperature range of observed spin-glass transitions in the $Zn_{1-x}Mn_xTe$ series (Fig. 1).

Using density-functional theory, we are able to show that Mn has the greatest influence on Te p and d orbitals and as both p and d orbitals strengthen their interaction as the bands move away from the Fermi level, Zn is effectively ignored in the electronic system and the spin-glass state becomes more robust. It is expected that the hybridization of Mn d to Te p orbitals creates a metastable state which can facilitate the spin-glass behavior. While pd hybridization is expected due to the magnetic impurities of the system, the overall "reach" of the interactions are compromised at low concentrations. This is illustrated in the findings of Mahmood *et al.* [12]. However, above $x = 0.20$, the orbital interactions are becoming more global.

Therefore, the incorporation of Mn into the ZnTe matrix produces a distinct pd-orbital hybridization through the Te, where this hybridization is activated when the Mn doping is above 0.20–0.25 concentration. The spin-glass transition temperature diagram (shown in Fig. 1) clearly indicates a shift in slope around $x = 0.20$, where the transition temperature trend is enhanced above that of the insulating spin-glass materials and increases dramatically for the DMS materials. The onset of the hybridization around the 0.25 doping level appears to happen simultaneously with the rise the spin-glass transition temperature. It seems likely that the coupling of pd-orbital hybridization of the Mn and Te p orbitals is a precursor to the enhancement of the spin-glass transition temperature.

While the spin-glass transition point has been investigated quite a bit over the last few decades, the onset of the spin-glass phase is typically correlated with an empirical and more general percolation threshold [1] around $x = 0.15$–0.30 doping concentration [2]. However, the data presented here illustrates a microscopic picture that can help shed light on the fundamental interactions that relate the dramatic shift in transition temperature to the occupying of p and d orbitals.

ACKNOWLEDGMENTS

A.A. and J.T.H. acknowledge support by the Institute for Materials Science at Los Alamos National Laboratory. T.M.P. acknowledges support from the UNF Terry Presidential Professorship, the UNF Office of Undergraduate Research, the Florida Space Grant Consortium, and by the National Science Foundation (NSF) Grants No. DMR-16-26332 and No. DMR-14-29428.

[1] J. Mydosh, *Spin Glasses: An Experimental Introduction* (Taylor & Francis, New York, 1993).

[2] K. H. Fischer and J. A. Hertz, *Spin Glasses*, Cambridge Studies in Magnetism (Cambridge University Press, Cambridge, UK, 1991).

[3] L. Personnaz, I. Guyon, and G. Dreyfus, Information storage and retrieval in spin-glass like neural networks, J. Phys. Lett. **46**, 359 (1985).

[4] A. Cruz, J. Pech, A. Tarancón, P. Téllez, C. L. Ullod, and C. Ungila, SUE: A special purpose computer for spin glass models, Comput. Phys. Commun. **133**, 165 (2001).

[5] O. Yoshitomo, Y. Mengjie, K. Jae, J. Xingchen, Z. Yun, Y. Bok, L. Michal, and A. Gaeta, Demonstration of chip-based coupled degenerate optical parametric oscillators for realizing a nanophotonic spin-glass, Nat. Commun. **11**, 4119 (2020).

[6] K. Binder and A. P. Young, Spin glasses: Experimental facts, theoretical concepts, and open questions, Rev. Mod. Phys. **58**, 801 (1986).

[7] D. L. Stein and C. M. Newman, *Spin Glasses and Complexity Volume 4 of Primers in Complex Systems* (Princeton University Press, Princeton, NJ, 2013), Vol. 4.

[8] H. Bellakhder, A. Outzourhit, and E. L. Ameziane, Study of ZnTe thin films deposited by r.f. sputtering, Thin Solid Films **382**, 30 (2001).

[9] P. Gibbs, T. M. Harders, and J. H. Smith, The magnetic phase diagram of CuMn, J. Phys. F **15**, 213 (1985).

[10] L. E. Wenger and P. H. Keesom, Magnetic ordering of $Au_{0.92}Fe_{0.08}$: A calorimetric investigation, Phys. Rev. B **11**, 3497 (1975).

[11] M. C. Massey, I. Manuel, P. S. Edwards, D. Parker, T. M. Pekarek, and J. T. Haraldsen, Magnetic impurity bands in $Ga_{1-x}Mn_xS$: Towards understanding the anomalous spin-glass transition, Phys. Rev. B **98**, 155206 (2018).

[12] Q. Mahmood, M. Hassan, and M. A. Faridi, Study of magnetic and optical properties of ZnTMTe (TM=Mn, Fe, Co, Ni) diluted magnetic semiconductors: First principles approach, Chin. Phys. B **26**, 027503 (2017).

[13] N. Benkhettou and D. Bensaid, First principles investigation of ferromagnetism for ZnMnY(Y=S, Se, Te), Open Condens. Matter Phys. J. **1**, 29 (2008).

[14] R. Bucker, H. E. Gomlich, and M. Krause, The influence of the temperature and the composition on the reflectivity of $Cd_{1-x}Mn_xTe$ within the spectral range of 1.5 eV $\leqslant$ E $\leqslant$ 4 eV, J. Phys. C: Solid State Phys. **18**, 661 (1985).

[15] K. Mayrhofer, K. Hochberger, and W. Gebhardt, The temperature and pressure dependence of the $3d^5$ transitions in $Zn_{1-x}Mn_xS$, J. Phys. C: Solid State Phys. **21**, 4393 (1988).

[16] A. Mauger, N. S. Almeida, and D. L. Mills, Magnetic polarons and electronic structure in semimagnetic superlattices: Application to CdTe/$Cd_{1-x}Mn_xTe$, Phys. Rev. B **38**, 1296 (1988).

[17] S. Oseroff, Magnetic susceptibility and EPR measurements in concentrated spin-glasses: $Cd_{1-x}Mn_xTe$ and $Cd_{1-x}Mn_xSe$, Phys. Rev. B **25**, 6584 (1982).

[18] L. Lundgren, P. Svedlindh, P. Nordblad, and O. Beckman, Dynamics of the Relaxation-Time Spectrum in a CuMn Spin Glass, Phys. Rev. Lett. **51**, 911 (1983).

[19] S. Nagata, P. H. Keesom, and H. R. Harrison, Low-dc-field susceptibility of CuMn spin-glass, Phys. Rev. B **19**, 1633 (1979).

[20] H. J. Masterson, J. G. Lunney, and J. M. D. Coey, Investigation into the magnetic properties of $Zn_{1-x}Mn_xTe$ thin films by the Faraday effect, J. Appl. Phys. **81**, 799 (1997).

[21] T. M. Pekarek, E. M. Watson, P. M. Shand, I. Miotkowski, and A. K. Ramdas, Spin-glass ordering in the layered III-VI diluted magnetic semiconductor $Ga_{1-x}Mn_xS$, J. Appl. Phys. **107**, 09E136 (2010).

[22] P. M. Shand, A. D. Christianson, L. S. Martinson, J. W. Schweitzer, T. M. Pekarek, I. Miotkowski, and B. C. Crooker, Spin glass behavior of $Zn_{1-x}Mn_xTe$, J. Appl. Phys. **79**, 6164 (1996).

[23] H. Maletta and W. Felsch, Insulating spin-glass system Eu_xSr_{1-x}, Phys. Rev. B **20**, 1245 (1979).

[24] D. Scalbert, J. Cernogora, and C. A La Guillaume, Spin-lattice relaxation in paramagnetic CdMnTe, Solid State Commun. **66**, 571 (1988).

[25] Y. F. Vaksman, Y. A. Nitsuk, V. V. Pavlov, Y. N. Purtov, A. S. Nasibov, and P. V. Shapkin, Optical absorption and chromium diffusion in ZnSe single crystals, Semiconductors **41**, 660 (2005).

[26] F. Ma, W. Ji, J. Hu, Z.-Y. Lu, and T. Xiang, First-Principles Calculations of the Electronic Structure of Tetragonal α-FeTe and α-FeSe Crystals: Evidence for a Bicollinear Antiferromagnetic Order, Phys. Rev. Lett. **102**, 177003 (2009).

[27] M. D. Watson, T. K. Kim, A. A. Haghighirad, N. R. Davies, A. McCollam, A. Narayanan, S. F. Blake, Y. L. Chen, S. Ghannadzadeh, A. J. Schofield, M. Hoesch, C. Meingast, T. Wolf, and A. I. Coldea, Emergence of the nematic electronic state in FeSe, Phys. Rev. B **91**, 155106 (2015).

[28] S. Takele and G. R. Hearne, Magnetic-electronic properties of FeS and Fe_7S_8 studied by ^{57}Fe Mossbauer and electrical measurements at high pressure and variable temperatures, J. Phys.: Condens. Matter **13**, 10077 (2001).

[29] K. Watanabe, K. Uchida, and N. Miura, Magneto-optical effects observed for GaSe in megagauss magnetic fields, Phys. Rev. B **68**, 155312 (2003).

[30] Z. Li, M. Liu, Q. Chen, Y. Huang, C. Cao, and Y. He, The electronic structure of GeSe monolayer with light nonmetallic elements decoration, Superlattices Microstruct. **109**, 829 (2017).

[31] T. LaMartina, J. Zhu, A. Balatsky, and J. Haraldsen, Dirac nodes and magnetic order in M_2X_2 transition-metal chalcongenides, Phys. Status Solidi RRL **12**, 1800181 (2018).

[32] J. S. Senoussi, New information on the spin-glass state of AuFe from transport measurements, J. Phys. F: Met. Phys. **10**, 2491 (1980).

[33] M. Simmons, H. A. Allak, A. Brinkman, and K. Durose, ZnTe/CdTe/CdS and ZnTe/CdTe/GaAs p-i-n solar cell structures grown by metalorginic vapour phase epitaxy, J. Cryst. Growth **117**, 959 (1992).

[34] H. Mertins, H. E. Gumlich, and C. Jung, Bandgap of $Zn_{1-x}Mn_xTe$: Nonlinear dependence on composition and temperature, Semicond. Sci. Technol. **8**, 1634 (1993).

[35] S. Smidstrup, T. Markussen, P. Vancraeyveld, J. Wellendorff, J. Schneider, T. Gunst, B. Verstichel, D. Stradi, P. Khomyakov, and U. Vej-Hansen, Quantumatk: An integrated platform of electronic and atomic-scale modelling tools, J. Phys: Condens. Matter **32**, 015901 (2020).

[36] QuantumATK version Q-2018.6, Synopsys QuantumATK (www.synopsys.com/silicon/quantumatk.html).

[37] N. Gonzalez Szwacki, E. Przezdziecka, E. Dynowska, P. Boguslawski, and J. Kossut, Structural properties of MnTe, ZnTe, and ZnMnTe, Acta Phys. Pol. A **106**, 233 (2004).

[38] R. Beaulac and D. R. Gamelin, Two-center formulation of Mn^{2+}-electron $s-d$ exchange coupling in bulk and quantum-confined diluted magnetic semiconductors, Phys. Rev. B **82**, 224401 (2010).

[39] L. Craco, M. S. Laad, and E. Müller-Hartmann, Ab initio description of the diluted magnetic semiconductor $Ga_{1-x}Mn_xAs$: Ferromagnetism, electronic structure, and optical response, Phys. Rev. B **68**, 233310 (2003).

[40] A. N. Andriotis and M. Menon, Universal features underlying the magnetism in diluted magnetic semiconductors, J. Phys.: Condens. Matter **30**, 135803 (2018).

[41] S. K. Nayak, M. Ogura, A. Hucht, H. Akai, and P. Entel, Monte Carlo simulations of diluted magnetic semiconductors using *ab initio* exchange parameters, J. Phys.: Condens. Matter **21**, 064238 (2009).

[42] S. Kervan and N. Kervan, First-principles study on half-metallic ferromagnetism in the diluted magnetic semiconductor (DMS) $Al_{1-x}Mn_xP$ compounds, J. Magn. Magn. Mater. **382**, 63 (2015).

[43] A. N. Andriotis and M. Menon, Successive spin polarization contribution to the magnetic coupling in diluted magnetic semiconductors: A quantitative verification, J. Magn. Magn. Mater. **501**, 166313 (2020).

[44] A. Bhattacharjee, G. Fishman, and B. Coqblin, Virtual bound state model for the exchange interaction in semimagnetic semiconductors such as $Cd_{1-x}Mn_xTe$, Physica B+C **117-118**, 449 (1983).